POLITECNICO DI TORINO
Repository ISTITUZIONALE

Bridging Thermally Induced Sintering Results with Preheating During Powder Bed Fusion with Electron Beam for -Ti21S

Original
Bridging Thermally Induced Sintering Results with Preheating During Powder Bed Fusion with Electron Beam for -Ti21S / Rizza, G., Cordova, L., Saboori, A., Hryha, E., Galati, M.. - In: APPLIED SCIENCES. - ISSN 2076-3417. - ELETTRONICO. - 16:16(2026). [10.3390/app16168224]

Availability:
This version is available at: 11583/3017752 since: 2026-11-11T11:25:46Z

Publisher:
Multidisciplinary Digital Publishing Institute (MDPI)

Published
DOI:10.3390/app16168224

Terms of use:

This article is made available under terms and conditions as specified in the corresponding bibliographic description in the repository

Publisher copyright

(Article begins on next page)

13 November 2026

applied sciences

MDPI

Article

Bridging Thermally Induced Sintering Results with Preheating During Powder Bed Fusion with Electron Beam for β-Ti21S

Giovanni Rizza [1,*], Laura Cordova [2,3], Abdollah Saboori [1], Eduard Hryha [2] and Manuela Galati [1]

[1] Department of Management and Production Engineering (DIGEP), Integrated Additive Manufacturing Center (IAM@PoliTo), Politecnico di Torino, Corso Duca degli Abruzzi 24, 10129 Torino, Italy; abdollah.saboori@polito.it (A.S.); manuela.galati@polito.it (M.G.)
[2] Department of Industrial and Materials Science, Chalmers University of Technology, SE-41296 Gothenburg, Sweden; laura.cordova@upm.es (L.C.); hryha@chalmers.se (E.H.)
[3] E.T.S. de Ingeniería Aeronáutica y del Espacio, Universidad Politécnica de Madrid, Plaza Cardenal Cisneros 3, 28040 Madrid, Spain
* Correspondence: giovanni.rizza@polito.it

Abstract

The metastable β-phase Ti21S titanium alloy, characterised by its low Young's modulus, oxidation resistance, creep strength, and high biocompatibility, has potential applications in aeronautical and biomedical fields. Despite these advantages, its adoption in additive manufacturing (AM) processes, particularly powder bed fusion with electron beam (PBF-EB), remains limited. A critical aspect of PBF-EB is the sintering phenomenon during preheating, which influences powder behaviour, thermal dissipation, and part quality. Insufficient sintering leads to poor energy dissipation and charge accumulation, while excessive sintering compromises powder reusability. This study investigates the sintering conditions required to optimise the PBF-EB preheating step for Ti21S. Thermogravimetric (TG) apparatus was employed as a controlled thermal treatment system to conduct a preliminary screening of the influence of temperature on powder sintering over a range of 400 °C to 700 °C. Parallel experiments were conducted using a PBF-EB machine to evaluate sintering behaviour. Scanning electron microscopy (SEM) was used to analyse the degree of sintering, while powder reusability was assessed by comparing the morphology and flowability of virgin and reused powders. The results show that conventional thermal treatment and PBF-EB preheating produce different sintering responses, likely because of the localised and rapid energy deposition associated with electron-beam heating. Nevertheless, controlled thermal treatment may provide a preliminary screening method for identifying temperature ranges for subsequent PBF-EB optimisation.

Keywords: sintering; EBM; Ti alloy; processing temperature; powder reusability

Check for updates

Academic Editor: Nicanor Cimpoesu

Received: 30 June 2026
Revised: 8 August 2026
Accepted: 12 August 2026
Published: 18 August 2026

Copyright: © 2026 by the authors. Licensee MDPI, Basel, Switzerland. This article is an open access article distributed under the terms and conditions of the Creative Commons Attribution (CC BY) license.

1. Introduction

The β-Ti21S is a titanium alloy originally designed for aeronautical applications when processed with traditional subtractive or forming processes [1]. In recent years, beta titanium alloys have been considered for biomedical applications as good candidates to replace the most common alpha-beta titanium alloys, such as Ti6Al4V [2]. Compared to the alpha-beta alloys, beta alloys are characterised by a reduced Young modulus (50 GPa < E < 100 GPa) [3], which prevents the stress shielding phenomenon when the bone is coupled to the implant [4–7]. Beta alloys are also characterised by a reduced presence of potentially cytotoxic elements in the alloy, such as vanadium, excellent corrosion resistance and good biocompatibility [8–13].

These advantages can be further enhanced if these alloys are processed using additive manufacturing (AM) techniques [9,14]. The unique layer-by-layer approach to component production would enable components with the specific designs required for applications in the aeronautical and biomedical sectors. However, the β-Ti21S titanium alloy has been rarely considered for production with AM techniques, probably because of its high sensitivity to the working thermal conditions [15].

Among the existing AM techniques, powder bed fusion with electron beam (PBF-EB) is one of the most used [16–18]. In PBF-EB, an electron beam serves as a primary energy source for processing the feedstock material in the form of powder particles. Due to the presence of the electron beam, the process needs to be conducted in a vacuum (approximately 10^{-3} mbar in the build chamber and 10^{-5} mbar in the electron beam column) to avoid interference between the air molecules and the electrons [19–22]. In addition, electrons may build a negative charge in the powder bed and produce the so-called smoke [23]. To prevent this, PBF-EB is a hot process in which each layer is preheated before melting. The high temperature stabilises the powder bed by triggering sintering phenomena between the powder particles [24,25]. To maintain a high ambient temperature, the start plate is preheated using the electron beam to a specific temperature, depending on the processed material [26]. When the target temperature is achieved, a thin layer of powder is raked on the start plate and preheated. During the preheating step, the electron beam is highly defocused and scanned at high speed (~15,000 mm/s) and current (~30 mA) [27]. For the Arcam machine, preheating is performed in two steps: preheating 1 and preheating 2 [28]. During preheating 1, the electron beam scans the square area that includes all the components that are going to be melted. During preheating 2, the electron beam scans an offset of the cross-section of each component to be melted. The beam parameters adopted for preheating are dependent on the material being processed and the targeted degree of powder sintering. After the preheating steps, the electron beam is focused to melt the cross-section of the components [29]. All these steps are repeated until the complete production of the components.

In the PBF-EB process, both the interaction between the electron beam and the powder bed and the overall thermal conditions within the build chamber play crucial roles. The electrons hit the surface of the powder particles, and the heat generated by the dissipation of the kinetic energy diffuses through the powder particles [30,31]. This determines a unique dynamic of powder heating and melting. The powder particles undergo different heating cycles depending on the process phase. Preliminary heating occurs when the powder is spread on the previous substrate (raking phase [32]). This thermal transfer occurs by heat conduction between the preheated start plate and previously melted material and particles. Subsequently, the powder bed in a PBF-EB, as mentioned above, is preheated by the electron beam. The typical temperature during this phase triggers sintering phenomena that are usually prescribed to avoid the smoke [23]. Sintering aims to form a solid bridge of material, identified as a neck [32]. The sintering phase and neck size influence the electrical and thermal properties of the powder bed [33], which, in turn, define the process safety and stability and, by controlling heat dissipation after melting, the microstructure of the components. The preheating step can be considered unproductive, and it should be performed as fast as possible and at the lowest temperature that prevents smoke or the precipitation of undesired phases in the alloy [34]. For these reasons, precise control of the energy provided by the electron beam and the temperature of the powder bed is required to manage this step efficiently. During the PBF-EB process, although there is no direct control over the layer temperature, a thermocouple placed below the start plate monitors the build temperature. During start plate heating, the temperature rises to the target temperature. For the PBF-EB processes, the user has direct control over the start plate heating, setting

the duration or temperature of preheating and the preheating parameters. The parameters for start plate heating are similar to those of preheating described above. The vacuum environment, the preheating step and the heat supplied during the melting step should maintain a stable temperature. If the thermal balance is not achieved with these phases, an additional heating phase follows the melting phase, known as post-heating [35]. The duration of post-heating is adjusted according to a parameter named "surface temperature". The software adjusts the duration of post-heating to align the temperature of the top-most layer with the set surface temperature. Hence, if the energy supplied during preheating and melting is too large, the post-heating may also be a cooling step. However, the post-heating duration is estimated by an internal control of the machine based on the heat previously supplied to the layer.

The preheating step and temperature control become increasingly important when processing alloys with mechanical properties that are dependent on microstructure, such as the β-Ti21S alloy considered in this work. Studies are available in the literature on processing this alloy with powder bed fusion using the laser beam [2,14,15], while processing this alloy with the PBF-EB has been shown only in Takase et al. [36] and Sun et al. [37]. The results of these works show that processing the β-Ti21S alloy with the PBF-EB process produces an α + β titanium microstructure, which has a detrimental effect on the mechanical properties of this alloy. Takase et al. [36] suggested a strong connection between the microstructure of the parts and the thermal history during the PBF-EB process. However, these studies provide no information on optimising the preheating step for this alloy. Owing to the high sensitivity of Ti21S to temperature and, therefore, the preheating parameters, controlled thermal-treatment experiments may provide preliminary information to select a temperature range to investigate in PBF-EB trials [38]. These could provide valuable insights into the thermal behaviour and sintering kinetics of powders, which are unfeasible to observe during the PBF-EB process. Although the application of thermal treatment experiments in this context has been widely explored for other powder metallurgy processes [39,40] to analyse the influence of process atmosphere [41], the sintering temperature, and time on the development of powder sintering necks, its utilisation in the optimisation of preheating for PBF-EB remains absent. The most widely adopted approach in the literature is trial and error, where the preheating parameters are adjusted to process the material safely without smoke [42]. Other studies investigated the effects of process parameters on sintering using an experimental approach [22] or numerical modelling with phase-field simulations [32].

In addition to controlling the process through preheating to prevent smoke, as mentioned above, sintering creates a solid bond between the particles. Specifically, parts produced by PBF-EB are embedded in a softly agglomerated mass of solid particles, known as the cake [21,43]. The components and powder connections must be freed using mechanical actions, such as blasting, using the same powder as the process [44]. This operation is performed in the so-called Powder Recovery System (PRS). The connection and its breakage could affect powder reusability by modifying particle size. Also, during reuse, the oxide layer covering the powder particles can change [45,46], which can modify the sintering and melting conditions as well as the physical properties of the powder particles, such as packing density and flowability [47].

The effect of powder reuse in PBF-EB has been extensively studied, particularly for the Ti6Al4V alloy [48,49]. Powder reuse can modify particle morphology, making the particles less spherical and increasing surface roughness. However, due to the reduction in satellites on the particles and the narrowing of particle size distribution, flowability tends to improve [50]. Additionally, small amounts of oxygen may be absorbed during the reuse cycle, increasing the hardness of the material [51].

Strategies involving the rejuvenation [52,53] of powder recovered through the PRS, such as adding virgin or new powder to the reused material, can help maintain key properties like particle size distribution. Other powder reuse strategies, including sieving, blending, and drying, can also influence the so-called powder spreadability [54], or the ability of the powder to be applied homogeneously in a thin layer. Existing studies on the impact of powder reuse in PBF-EB reveal that changes in powder properties can affect part quality. However, with the implementation of effective reuse strategies and continuous monitoring, potential negative impacts can be mitigated, ensuring consistent processability and part quality.

In light of the limited information available in the current literature, this study preliminarily leverages controlled thermal treatment experiments to systematically investigate the sintering behaviour of β-Ti21S powders, aiming to optimise the preheating phase in PBF-EB. The study examines whether controlled thermal treatment can support preliminary screening of powder sintering behaviour before process-specific PBF-EB optimisation and considering also the material reusability. To the best of the authors' knowledge, this is the first study to explore Ti21S powder reusability in the PBF-EB process.

2. Materials and Methods

This work focuses on the characterisation and the identification of the suitable preheating temperature for the metastable β phase Ti21S (Ti-15Mo-2.9Nb-3Al-0.2Si) powder. The material was supplied by GKN Ltd., Redditch, England, UK and the chemical composition is listed in Table 1. According to the manufacturer's datasheet, the powder was characterised by a particle size distribution of D_{10} = 59 μm, D_{50} = 78 μm and D_{90} = 106 μm.

Table 1. Chemical composition in wt. % of the β-Ti21S alloy adopted in this work.

Element	Composition
Aluminium	3.1%
Molybdenum	15.2%
Carbon	0.01%
Silicon	0.23%
Iron	0.01%
Nitrogen	0.01%
Hydrogen	0.001%
Oxygen	0.11%
Niobium	2.92%
Titanium	Balance

2.1. Preheating Temperature Analysis

In the PBF-EB process, the start plate is placed floating on the unprocessed feedstock material. The thermocouple adopted to estimate the start plate temperature is placed in contact with the face of the start plate immersed in the powder. Figure 1 shows a typical temperature profile recorded from the thermocouple. The PBF-EB process starts with the preheating of the start plate. The electron beam is repeatedly scanned on the start plate, and its temperature increases until it reaches a target value that depends on the processed material. When this temperature is achieved, the start plate is lowered, and a layer of powder is raked onto it. The new layer of powder is then preheated with a series of electron beam scans. After the deposition of the first layer of powder, usually, the temperature read from the thermocouple begins to drop. This is because the powder under and surrounding the start plate sinters and begins to disperse the heat accumulated in the initial step. The temperature smoothly drops to a value that should remain approximately constant throughout the build. This is because a balance is achieved between the energy provided by the

electron beam and the heat dispersed in the environment. This condition can be considered healthy, where the powder is properly sintered and the build environment conditions are optimal for production, ensuring proper connection size and thermal and electrical conductivity. However, changes in the thermocouple temperature reading could indicate that something in the process is not working properly. A constant drop in temperature, also while processing the material, indicates that the powder is not sufficiently sintered and is not adequately sintered to the start plate. The energy provided by the electron beam is dispersed slowly, accumulating heat in the last processed layer. This indicates that the temperature of the current layer could be higher than the temperature recorded by the thermocouple. On the other hand, if the temperature increases, it indicates that the powder is over-sintered. The energy provided during the preheating step is directly transferred to the start plate and dispersed, resulting in a current-layer temperature that could be too low. This could lead to smoke phenomena. The stability of the PBF-EB depends on an adequate processing temperature, which controls the degree of powder bed sintering and, consequently, the formation of interparticle necks. These necks determine the effective thermal and electrical conductivity within the powder bed and ensure reliable particle-to-particle connectivity, which is essential to prevent smoke phenomena during processing. This stability is usually achieved using a trial-and-error approach. In the common procedure, a build is conducted with only material preheating. The energy provided during preheating is gradually reduced until the smoke phenomenon starts to happen. The procedure then stops, considering the parameters before smoke as the best for powder processing.

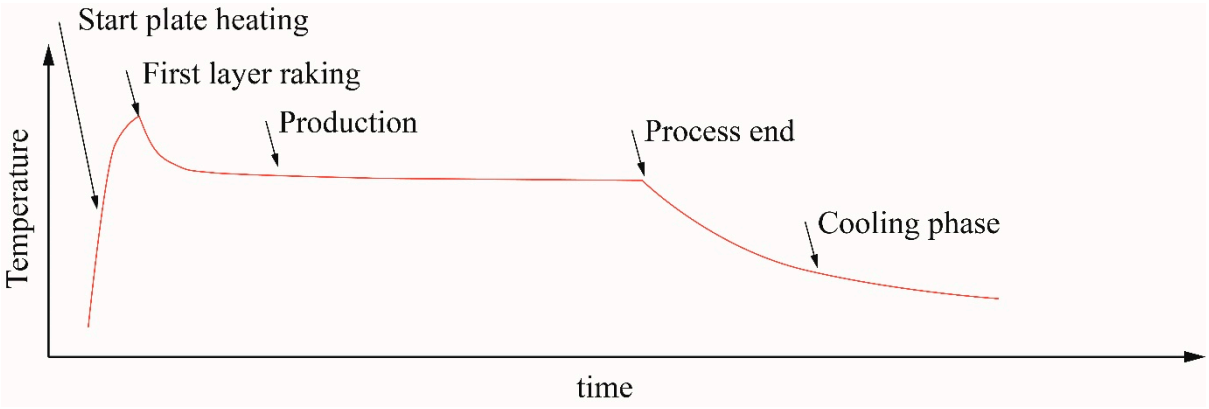


Figure 1. Temperature profile measured by thermocouple, with the principal phases where temperature changes.

Prior to the experimental approach, this work proposes an analysis based on thermal simulation and thermal treatment experiments to identify a suitable working temperature for the PBF-EB. The phase composition and stability during sintering were simulated using the CALPHAD (CALculation of PHAse Diagrams) methodology with the ThermoCalc software v.2022b and TCTI4: Ti-Alloys v4.0 database. According to the results of this preliminary simulation, sintering experiments were performed using a thermogravimetric (TG) thermal analyser STA449 (NETZSCH Thermal Analysis GmbH, Bayern, Germany). Powder samples of 2 g were heated from room temperature to 400 °C, 500 °C, 600 °C and 700 °C with a heating rate of 10 °C/min followed by an isothermal hold for 2 min and a cooling rate of 30 °C/min, under vacuum conditions (10^{-4} mbar). After the sintering experiments, the powder was examined with the high-resolution scanning electron microscopy (HR-SEM) using a Carl ZEISS-LEO Gemini 1550 SEM microscope (ZEISS Microscopy, Jena, Germany), equipped with a field emission gun to analyse the degree of sintering. This analysis shows the impact of temperature on the degree of sintering neck formation. This

has been experimentally verified by performing the following tests in a PBF-EB machine, Arcam A2X (Colibrium Additive, a GE Aerospace company, West Chester, OH, USA).

In the PBF-EB machine, three tests, corresponding to three builds, consisted only of powder sintering (no melting was realised). However, the machine control does not allow a build without a melting step. Therefore, a dummy cube was positioned in the centre of the start plate. The melting step was performed at a low current (1.5 mA) and high speed (speed function set to −1000) to prevent material melting. Another condition imposed by the machine is defining the preheating area and the target surface temperature. The first parameter specifies the area that will be subjected to the preheating, while the second parameter controls the post-heating phase.

For these three builds, the preheating area was set equal to a square of 145 mm on a side for the first and second builds and a square of 190 mm on a side for the third build. For all the builds, the layer thickness was equal to 0.050 mm. The machine was prepared following the standard procedure for the Arcam A2X, placing a start plate on a 40 mm layer of unprocessed powder. The thermocouple was placed in direct contact with the side of the start plate immersed in the powder. This thermocouple was the only device used to measure the start plate temperature, and the reading may be influenced by misplacement and a lack of contact with the start plate surface during machine preparation. Hence, the temperature measurement provided by the thermocouple can be considered only an indication rather than an accurate measure of the exact temperature on the top side of the start plate. For this reason, using temperature as a condition for distributing the first layer of powder and starting production may introduce error due to inconsistent machine preparation. Preliminary tests were performed on the start plate to identify the parameters and the time required to reach the prescribed temperature before the powder spreading. The preheating of the start plate was controlled in time, so that the raking of the first powder layer starts independently of the temperature measured by the thermocouple. The start plate used for these builds, provided by Arcam, was made of stainless steel and measured 210 mm × 210 mm × 10 mm. The powder was distributed using the triple-pass method, where the powder is fetched and distributed on the build area, and then the rake passes on the build area two more times to level the powder bed before preheating starts.

The selection of parameters related to temperature during PBF-EB will be clarified when discussing the results of the CALPHAD simulations.

During the first build, the start plate was preheated for 10 min. At the end of this time, the temperature read by the thermocouple placed below the start plate was approximately 350 °C. Table 2 reports the values of process parameters adjusted in the EBM control of the machine for the preheating and post-heating of the powder distributed on the start plate. The preheating area adopted for this build was a square with a side equal to 145 mm. For this build, the surface temperature was set to 400 °C. With this combination of process parameters, the post-heating lasted approximately 15 s for each layer.

Table 2. Preheating parameters for the first build.

Parameter	Preheating
Beam current [mA]	20
Beam speed [mm/s]	15,000
Number of repetitions	3
Preheating square side [mm]	145

The second build was conducted at higher temperatures than the first. The start plate was preheated for 30 min. At the end of the start plate heating, the thermocouple recorded a temperature of 670 °C. Table 3 reports the process parameters specified in the EBM Control

software (version 5.2.52) of the machine for the preheating and post-heating phases. Also, for this build, the preheating area was set to a square with a side length of 145 mm. The surface temperature for this build was set to 500 °C. With this surface temperature, the post-heating phase lasted approximately 15 s for each layer.

Table 3. Preheating parameters for the second build.

Parameter	Preheating
Beam current [mA]	28
Beam speed [mm/s]	10,000
Number of repetitions	4
Preheating square side [mm]	145

For the third build, the start plate was preheated for 30 min—as it was for the second build—but at the end of preheating the temperature was approximately equal to 730 °C. The parameters adopted for preheating of the powder layer were the same as those adopted for the first build, reported in Table 2. In this case, however, the preheating area was set as a square with side length equal to 190 mm. For this build, the surface temperature was set to 500 °C. With this temperature, the post-heating lasted approximately 17 s.

Table 4 summarises the temperatures and the post-heating durations of the series of PBF-EB builds.

Table 4. Process conditions of builds 1, 2 and 3 in the PBF-EB process.

Parameters	Unit	Build 1	Build 2	Build 3
Start plate temperature	[°C]	350	670	730
Surface temperature	[°C]	400	500	500
Post-heating duration	[s]	15	15	17

2.2. Powder Analysis and Characterisation

The particle surface morphology of the samples was studied by high-resolution scanning electron microscopy (HR-SEM) using a Carl ZEISS-LEO Gemini 1550 SEM microscope (ZEISS Microscopy, Jena, Germany), equipped with a field emission gun. The particle size distribution was measured by laser diffraction using a Mastersizer 2000 by Malvern Panalytical, Malvern, UK (according to ASTM B 822-02 [55]). The X-ray Diffraction (XRD), model X'Pert from Philips (PANalytical B.V., Almelo, The Netherlands), was performed using Bragg–Brentano optics with Cu-Kα radiation to identify the phases present in the alloy. The diffraction patterns were acquired over a 2θ angle range from 30° to 120° and processed using the X′ Pert HighScore Plus software, version 3.0. The X-ray tube was operated at 40 kV and 40 mA, and the diffraction patterns were recorded with a step size of 0.02° in 2θ and a counting time of 1 s per step. These measurements were performed on virgin and reused powder as well as sintered materials from the PBF-EB process extracted from the first, second and third builds.

At the end of each build, the powder followed the standard reuse process for the PBF-EB. The powder was extracted from the build chamber and broken down using sandblasting with the PRS system, using the same powder material. After disaggregation, the powder was sieved and used for subsequent builds. The reusability analysis was performed comparing virgin powder (collected as received from the producer) to a sample of powder extracted after the third build (collected after the sieving process).

To study the impact of reusing the Ti21S powder in the PBF-EB process, the rheological behaviour was tested. Samples of virgin and reused powder collected at the end of the third build were selected and tested by the rotation drum principle using a Revolution Powder

Analyzer (RPA) by Mercury Scientific Inc (Newtown, CT, USA). The test is carried out on a rotating and transparent drum filled with powder. A camera in front of a light source records pictures of the powder surface area during movement. The Revolution Powder Analyzer software, through the flowability module (Mercury Scientific Inc., Newtown, CT, USA), calculated powder flowability metrics such as cohesion, avalanche angle and break/avalanche energies. An equal sample size of 66 g of virgin and reused material was freely loaded in the drum. For the flowability measurements, a constant speed of 0.6 rpm was selected, in which 150 powder avalanches were analysed. Additionally, a separate experiment varying speed from 1 to 70 rpm was set in which 75 avalanches were analysed for each angular speed. The selection of the speed range was based on the rake linear speed of about 250 mm/s, which is equivalent to an angular speed of 48 rpm.

3. Results and Discussion

3.1. Preheating Temperature Study and Thermal Treatment Experiments

As mentioned above, the CALPHAD simulation prior to the sintering experiments using TG design of experiments helped select the preheating temperature range. Figure 2 shows the volume fraction of phases at different temperatures. During heating, the volume fraction of β phase with a body-centred cubic (BCC) crystal structure increases up to the β-transus temperature, which for this composition is above 800 °C (805 °C reported by [56]) when the α phase, having a hexagonal compact packing (HCP) crystal structure, disappears. The temperature range for the preheating step was selected between 350 °C (above the ω-solvus (350 °C [57]) and 700 °C. This range was chosen given the technical capabilities of the TG equipment and to ensure good processability in the PBF-EB machine with sintering between the powder layer and the start plate.

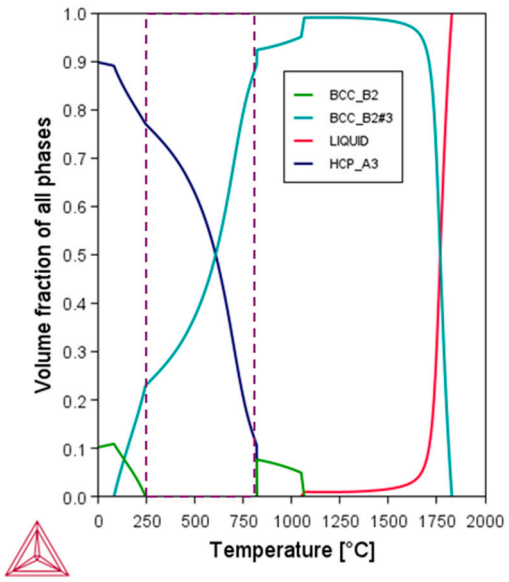


Figure 2. CALPHAD-predicted phase volume fractions as a function of temperature for the Ti21S alloy. In the phase labels, the suffix "#n" identifies compositionally different instances of the same phase.

The Ti21S powder was heat treated by a sintering experiment to simulate the preheating step in the PBF-EB machine. Four different temperatures: 400 °C, 500 °C, 600 °C and 700 °C were tested. Figure 3 presents SEM images of the powders recovered after the sintering experiments at 400 °C (Figure 3a,b), 500 °C (Figure 3c,d), 600 °C (Figure 3e,f), and 700 °C (Figure 3g,h). The extent of interparticle bonding was assessed qualitatively from the condition of the powder during recovery and from the agglomeration visible in the low-magnification SEM images (Figure 3a,c,e,g). After the crucible was turned over

a clean collection area, the powder treated at 400 °C was recovered in a loose condition. Consistently, Figure 3a shows predominantly dispersed and individually distinguishable particles, without mechanically stable agglomerates. By contrast, the powders treated at 700 °C (Figure 3g) retained agglomerate structures during recovery and handling, covering the entire area of the image. This is considered a qualitative indication of more extensive agglomeration. At higher magnification, the agglomerates appear as complex structures composed of multiple connected particles (Figure 3h). Although individual sintering necks cannot always be clearly resolved, the preservation of these structures during recovery and SEM sample preparation indicates the presence of interparticle bonding. These observations suggest that the interval between approximately 500 °C and 700 °C may be useful for preliminary screening for determining a PBF-EB processing window.

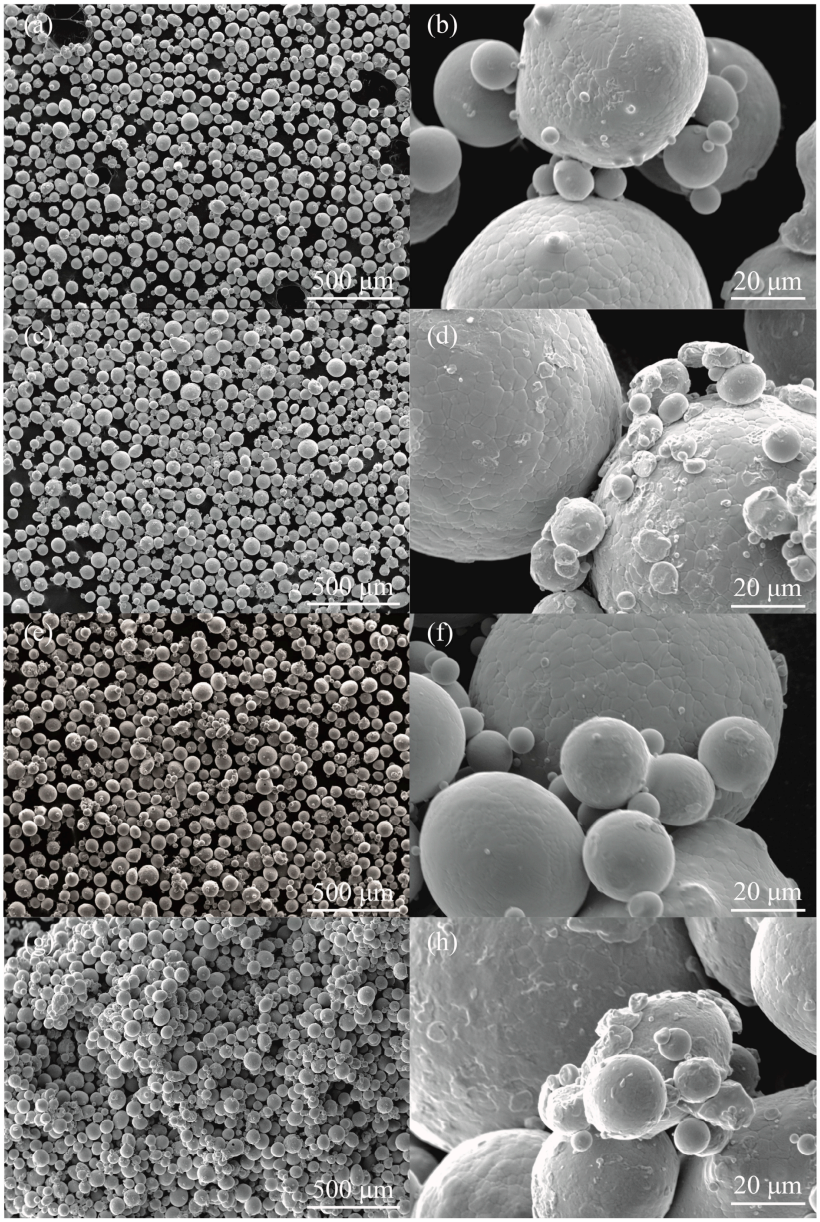


Figure 3. Powder morphology of agglomeration of particles after sintering experiments using TG apparatus at magnifications 100× (**a**,**c**,**e**,**g**) and 2000× (**b**,**d**,**f**,**h**), respectively at: 400 °C (**a**,**b**), 500 °C (**c**,**d**), 600 °C (**e**,**f**) and 700 °C (**g**,**h**).

3.2. Powder Processability by the PBF-EB Process

The different process conditions investigated in the series of three builds led to different results in terms of powder processability and sintering during the PBF-EB process. Figure 4 shows the temperature evolution recorded by the thermocouple positioned under the start plate for the three builds extracted from the log files produced by the machine. All three temperature evolutions follow the typical pattern during PBF-EB, as schematically shown in Figure 1. The curves for the three builds show the different maximum temperatures achieved at the end of start plate heating and the different build durations.

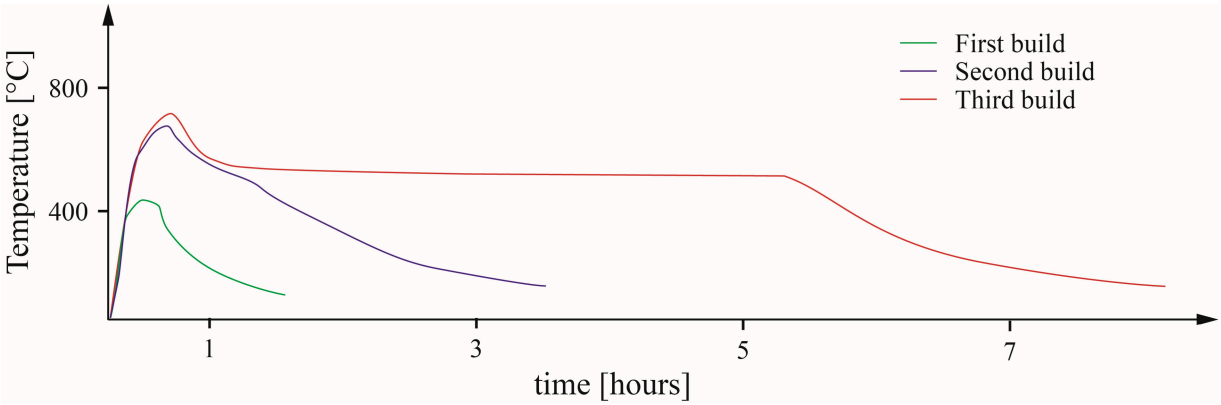


Figure 4. Temperature evolution during the builds measured by the thermocouple positioned under the start plate.

Figure 5 reports an image of the build chamber and the condition of the powder bed at the end of the first build. The combination of process parameters for the first build allowed for the safe processing of approximately 30 layers of powder. After these layers, a structure as thick as the total number of layers processed (approximately 1.5 mm) detached from the start plate and was spread inside the build volume by the rake.

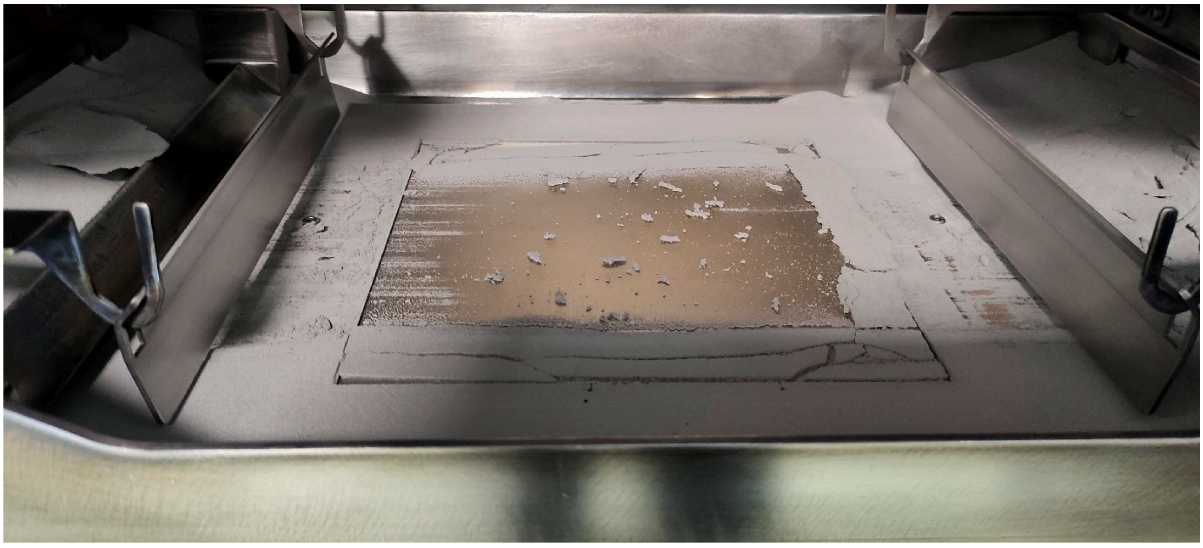


Figure 5. Build chamber with the deposited powder after the first build.

The result of this build shows that the process parameters are not suitable for conducting the process safely. While the start plate temperature was around 350 °C at the beginning of the process, the energy provided during subsequent preheating produced slight sintering of the powder particles and an increase in temperature, which remained below around

450 °C. Although the build was unsuccessful, these observations are qualitatively consistent with the sintering experiments in TG apparatus, in which a more evident interparticle bonding was observed from approximately 500 °C. As reported in the description of the process, during the PBF-EB, the temperature is measured using a thermocouple placed below the start plate. While the temperature at the end of the start plate heating may be considered representative of the overall temperature of the start plate, the thermal inertia of the start plate, which behaves as a heat accumulator, hinders an instantaneous measurement of the temperature of the powder layer. Therefore, the thermocouple response suggests that heat is accumulated during processing and therefore the actual powder bed surface temperature might be above 500 °C. Considering the temperature at the end of the start plate heating, this was not sufficient to allow the diffusion phenomena that bond the titanium powder particles on the stainless steel start plate, which, according to the literature, is approximately equal to 900 °C [58]. Owing to the reduced adhesion of the powder particles to the start plate, the heat generated by the impact of the electron beam on the powder bed accumulates in the powder particles, increasing the powder bed surface temperature. This produces a relatively strong sintering among the powder particles, in agreement with the sintering in TG apparatus experiments. The missing bonding between the sintered powder and the start plate, caused by the low start plate temperature at the start of the process, led to movement of the powder bed. However, the rapid sintering due to the overheating of the powder bed prevented the formation of strong connections between particles. As a result, even a gentle movement of the rake was sufficient to disrupt the powder bed.

Figure 6 shows the result of the second build. For this second build, only one layer was processed. After raking the powder layer and during the preheating step, the powder agglomerated, forming the structures that are visible in Figure 6.

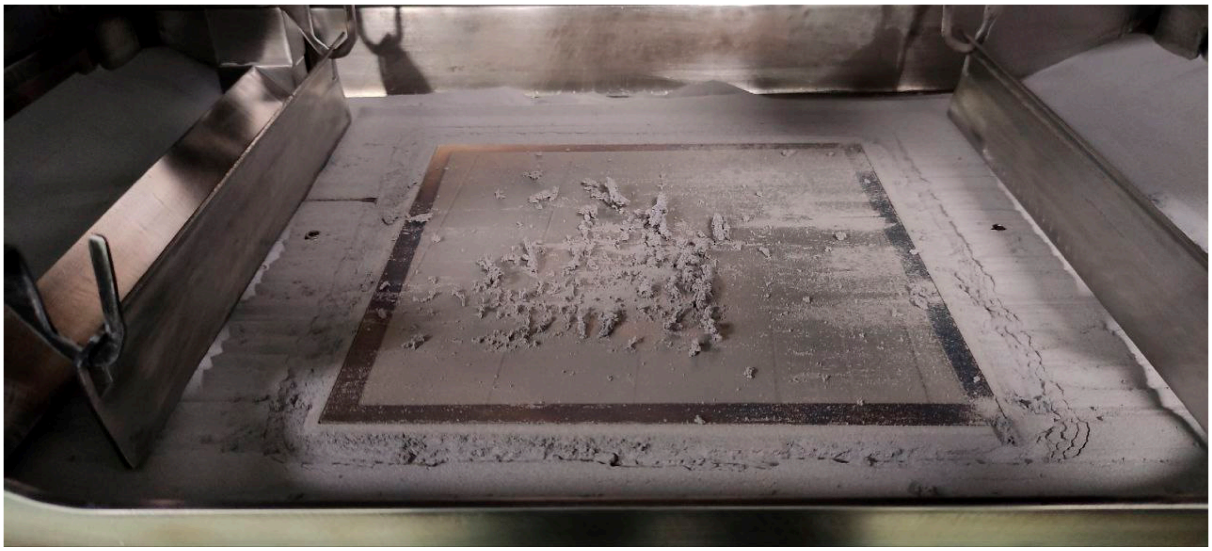


Figure 6. Build chamber with the deposited powder after the second build.

The phenomena that led to the formation of these structures are similar to those of the first build. As in the previous build, the temperature of the start plate was not high enough to allow the diffusion bonding of the powder to the start plate. Moreover, the use of a higher beam current and lower beam speed adopted for the preheating of the powder facilitated the sintering among the powder particles. While the temperature measured by the thermocouple at the end of the start plate heating remained below 670 °C, it is more likely that the temperature of the powder particles exceeded this temperature. This led to extensive

interparticle sintering in line with the sintering in TG apparatus experiments. Figure 7 shows the details of one of the structures extracted from the build chamber. The presence of necks among the powder particles is evident in Figure 7a. The image shows that the powder particles are spherical and strongly sintered. Figure 7b shows a detail of the neck among the powder particles. While the temperature was high enough to allow sintering among the powder particles, it was not high enough to allow adhesion to the start plate.

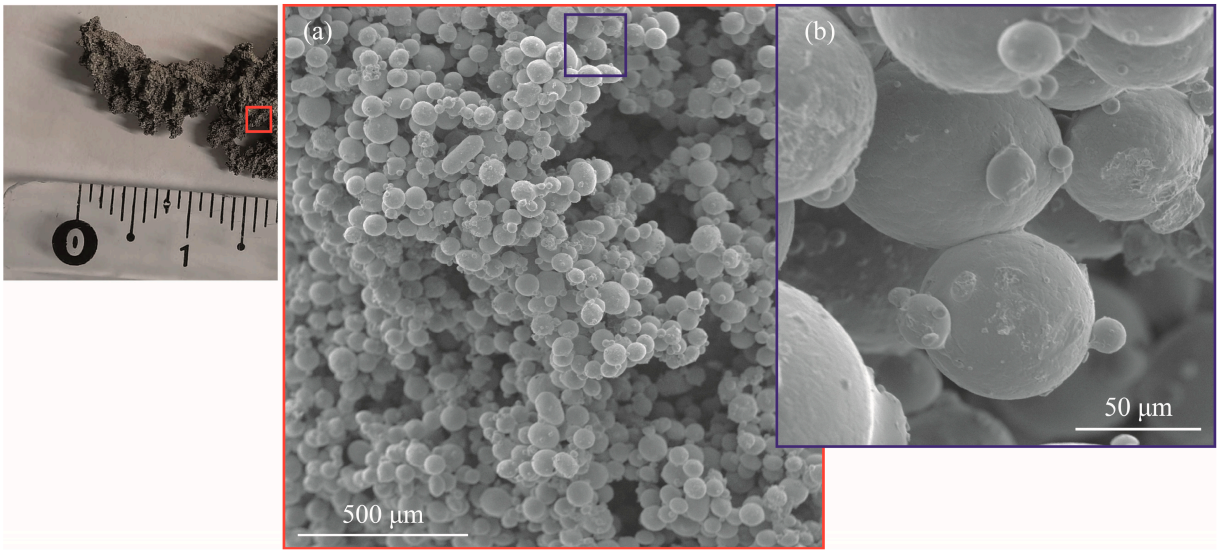


Figure 7. Agglomerated powder structure recovered from the build chamber after the second build: (**a**) Morphology of powder particles and (**b**) detail of the necking between two particles.

However, unlike the first build, the start plate temperature was higher, and the parameters adopted to preheat the powder provided more energy (Table 3). The formation of the agglomerates visible in Figure 7 could be the result of the triple passage of the rake. Another possible explanation could be the local phase transition from α (HCP) to β (BCC) inside the powder particle. This phase change, if occurring, might induce stresses due to changes in the crystallographic structure or the release of residual stresses. In this context, the precipitation of the α phase within grains and at grain boundaries observed during the ageing of β-phase powder in [59] illustrates the sensitivity of this alloy to its thermal history. The combined effects of repeated rake passage and increased thermal exposure may therefore have contributed to the agglomeration observed during the second build.

The process conditions adopted for the third build allowed the powder to be processed safely. With these process parameters, 540 layers were processed. Figure 8 shows the results of this build, in which a sintered cake of powder was obtained. For this build, at the end of the start plate heating, the thermocouple measured approximately 730 °C. This temperature is the highest temperature recorded for this series of builds. The high temperature and energy supplied during preheating of the powder layer enabled diffusion mechanisms to occur, thereby stabilising the powder layer, with the powder particles adhering to the start plate. When adding the other layers of material, the preheating parameters identified resulted in good sintering of the powder particles, enabling safe processing of the material. The compactness of the powder was initially evaluated by the operator, ensuring that this does not easily disaggregate. The powder block was subsequently transferred to the PRS and disaggregated using compressed air. A pressure of 4 bar was adopted to disaggregate the block, indicating that the powder bed had achieved sufficient consolidation to support a stable production process [60]. The selection of this preheating temperature considered not

only the β-transus temperature to maximise the β-phase fraction but also powder sintering and anchoring of the powder to the start plate.



Figure 8. Build chamber with the powder cake obtained after the third build.

The temperature adopted for the third build, however, while allowing the powder to be safely processed, was close to the β-transus temperature, which, for this alloy, as presented in Figure 2, is close to 800 °C. Keeping the material at such a high temperature for hours, as is common for the PBF-EB process, may lead to an α + β microstructure, as reported in [36].

The results of these experiments enable comparison between the sintering using the TG apparatus and PBF-EB techniques. Although the temperatures applied in the TG experiments and PBF-EB experiments were comparable, notable differences arose due to the distinct heating rates characteristic of each technique. In PBF-EB, the powder experiences extremely rapid heating, which in principle would suggest that slower heating in the TG apparatus should promote more effective sintering. However, this was not observed. The role of surface oxides must also be taken into consideration, as these layers need to be reduced or dissolved prior to sintering. In the case of Ti and Ti-based alloys, such oxides can dissolve into the metallic matrix under appropriate conditions [61].

However, one possible explanation for the different sintering behaviour is the difference in heat delivery between the two systems. Sintering using the TG apparatus relies on slow and uniform furnace heating, whereas PBF-EB heating is driven by an electron beam, which preferentially overheats the powder surface. This localised thermal input promotes oxide dissolution and generates sufficiently high sintering activity to form interparticle necks. Given that the selected temperatures and vacuum conditions were similar in both setups, these findings indicate that controlled thermal treatment in a TG apparatus may serve as a preliminary screening method for evaluating sintering behaviour and powder processability relevant to PBF-EB.

3.3. Powder Reusability

The powder as received from the supplier is labelled as ‘virgin’, and the powder that was used at least once before is labelled as ‘reused’. In this case, the powder used to build the ‘reused’ specimens had already been used for three cycles during the preheating studies. In this section, the powder particles of each condition are studied.

3.3.1. Powder Morphology and Particle Size Distribution

Figure 9 shows the morphology of the powder particles in virgin and reused conditions. No morphological differences were observed between the two materials. Both virgin and reused powder show particles relatively spherical, some of them with several satellites.

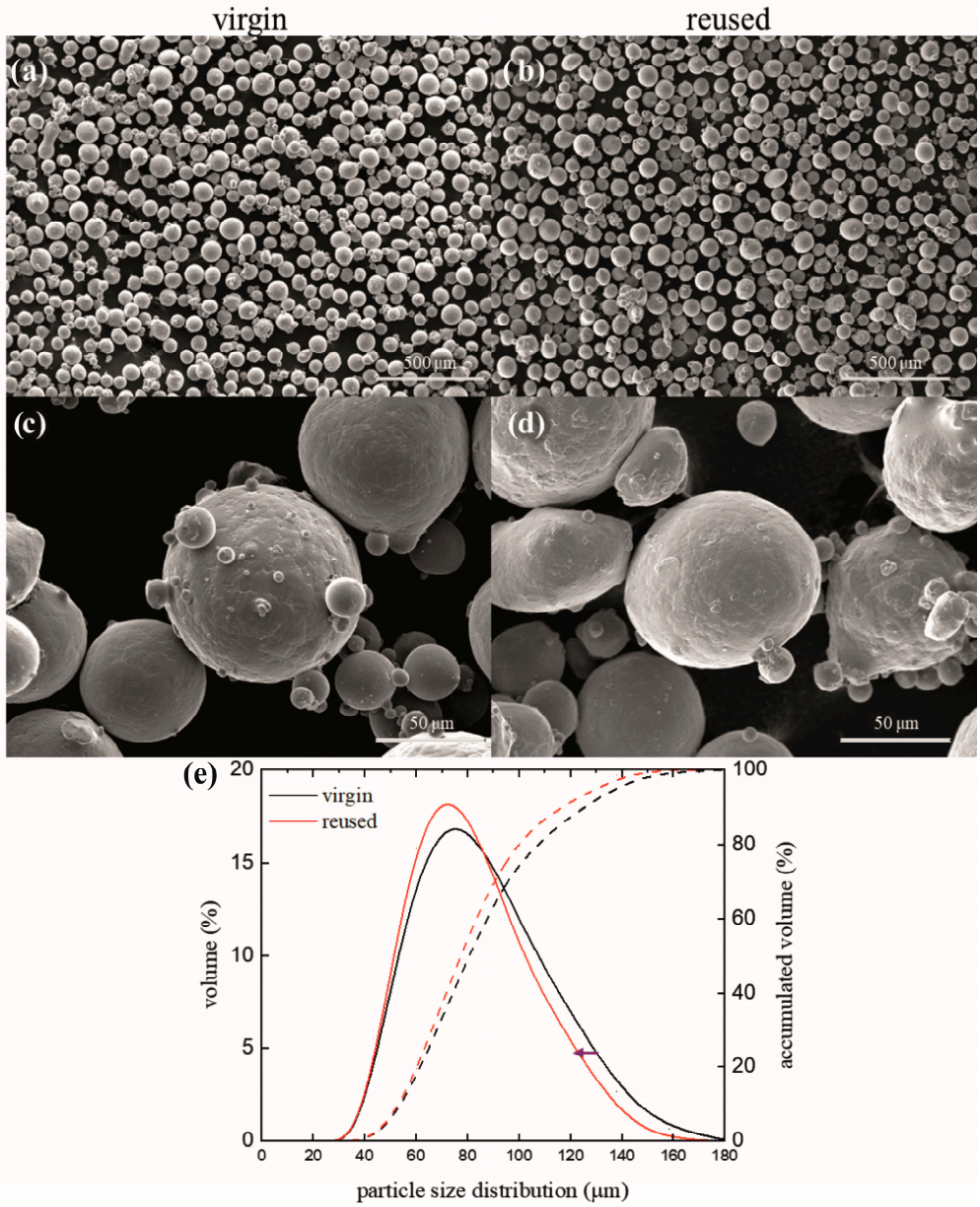


Figure 9. Powder morphology of virgin (**a**,**c**) and reused (**b**,**d**) powders, and their particle size distribution (**e**).

The particle size distribution in Figure 9e shows a slight refinement in the particle size during reuse, which is typically caused by the sieving process and reported by other authors who studied reusability of Ti6Al4V powder in PBF-EB [50], reporting a narrower PSD after 6 cycles of reuse. Table 5 shows that the PSD narrowing is mainly caused by a reduction in the coarser fraction of particles (D90). Even though the mesh size of the sieve used between cycles is 150 µm, allowing sieving particles up to this size, the sieving time and frequency used determine the efficiency of the method. Therefore, like in most powder-based AM methods, the powder reuse slightly modifies the PSD. This modification did not significantly compromise powder processability in the three builds investigated in Section 3.2. The reused powder maintained sufficient flowability for gravity-driven

delivery and the formation of uniform layers in the Arcam A2X system, as it remains within the range of powder fraction suitable for the PBF-EB process.

Table 5. Particle size distribution metrics of virgin and reused Ti21S powder.

Material	D10	D50	D90
virgin	54.4 µm	80.5 µm	119.2 µm
reused	53.6 µm	77.2 µm	110.9 µm

3.3.2. Phase Distribution

The XRD analysis confirms that the virgin powder is constituted by a single metastable β phase (Figure 10a). A weak reflection at approximately 40° is visible in the XRD patterns of the powder collected after the third build, as shown in the enlarged region in Figure 10a. The position of this reflection may be consistent with the α-Ti (101) reflection and could therefore suggest the presence of a minor α-Ti fraction. However, owing to the low intensity of the reflection and the absence of quantitative phase analysis, this assignment remains tentative and requires further investigation. If present, a minor α-Ti fraction in the reused powder would be expected to dissolve during powder melting in the subsequent PBF-EB process. Comparing the virgin powder with the powder sintered after the builds in the PBF-EB process (Figure 10b), the peaks show a decrease in relative intensity, which is a measure of variations in the crystallographic texture of the sintered particles. However, since the XRD patterns shown in Figure 10 were not normalised, the comparison focuses on peak positions and phase identification rather than absolute diffraction intensities. Similar observations on the phase constitution of this alloy were made by Pellizzari et al. [3].

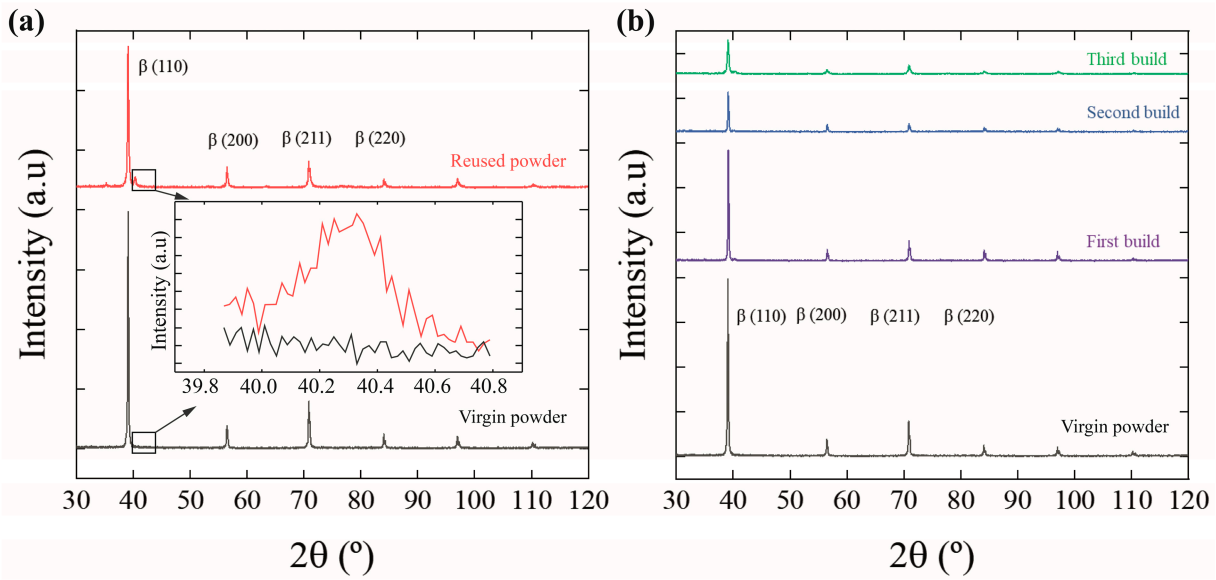


Figure 10. XRD patterns of β-Ti21S virgin and reused powder. (**a**) Comparison between virgin powder and powder reused after the three builds in the PBF-EB. (**b**) Comparison between the XRD patterns of virgin powder and the pattern for powder extracted after the first, second and third build in the PBF-EB.

3.3.3. Rheological Behaviour

The study of the rheological behaviour of metal powders is key to processability and reusability in PBF-EB. The application of a homogeneous thin layer before scanning by the electron beam ensures full contact between particles for higher electrical conductivity and, therefore, successful melting. The presence of surface imperfections on the particles, such as satellites,

oxides and impurities, could negatively impact the processability. In general, spreadability is a measure of the successful application of a thin layer of powder subjected to variations in particle morphology, PSD, phase and chemical composition and surface topography.

Figure 11 shows the parameters that characterise the rheological behaviour of virgin and reused Ti21S powders (GKN Ltd., Redditch, England, UK). The avalanche energy, break energy and cohesion at a constant speed of 0.6 RPM are shown in Figure 11a. At low speeds, the flowability parameters are quite similar, except for cohesion, which shows a higher value for the reused material. In fact, cohesion, which indicates whether the powder flows as individual particles or agglomerates, follows a similar trend at high rotation speeds, showing higher values for reused powders than for virgin powders, as shown in Figure 11d. The dynamic measurements with varying angular speeds between 10 RPM and 40 RPM show the avalanche angle is lower for reused powders than for virgin powders. The mechanisms governing changes around 10 RPM are due to transitions between slumping, rolling and cascading of the powder particles. It is worth mentioning that the relevant angular speed range in the PBF-EB process is around 40–50 RPM, coinciding with approximately 200 mm/s to 250 mm/s, linear speeds typically used in the layering process. In this range, both the avalanche angle (Figure 11c) and cohesion (Figure 11d) show variations in their values, with virgin powders exhibiting better flowability behaviour.

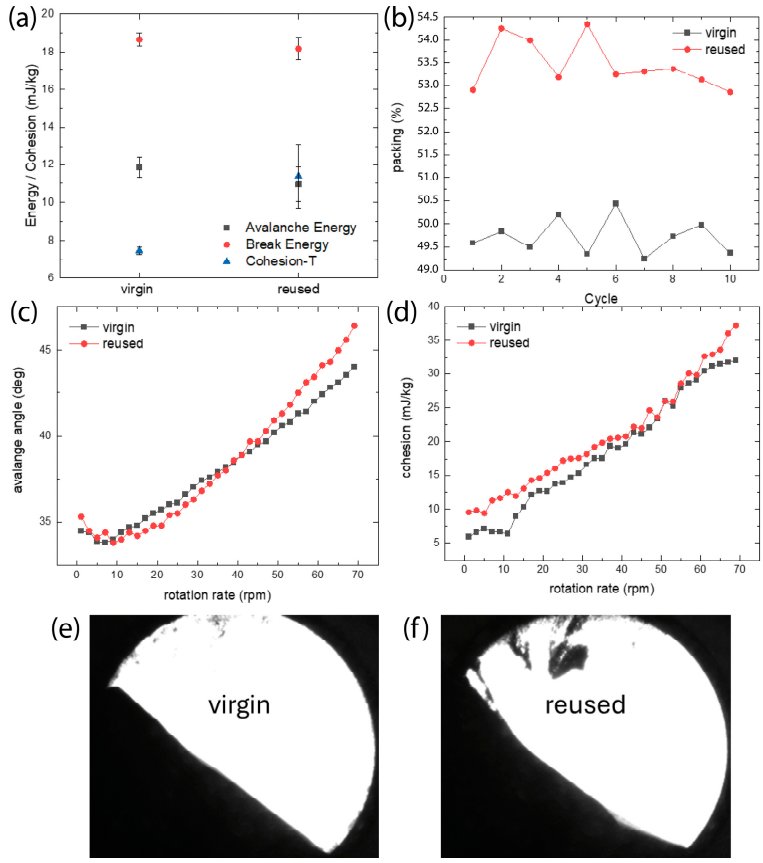


Figure 11. Rheological characterisation of virgin and reused powders: (**a**) flowability metrics, including avalanche energy, break energy, and cohesion, measured at a constant rotational speed of 0.6 rpm; (**b**) packing density; (**c**) avalanche angle; and (**d**) cohesion. Avalanche morphologies of the (**e**) virgin and (**f**) reused powders measured at 1 rpm.

Figure 11e,f show the powder avalanche morphology, which maintains a straight line. This is a measure of the excellent flow behaviour of the powder particles. This image was taken at a rotation speed of 1 RPM, at which the reused powder exhibits worse flowability than the virgin powder, as also indicated by a slight sticking behaviour of the powder. One

reason for this slight reduction in flowability might be moisture uptake during exposure to air. In fact, the virgin powder was stored in sealed cans. On the other hand, the reused powder was exposed to air while handling, in the PRS, and during sieving. This may produce the capture of atmospheric moisture, which reduces powder flowability.

Packing behaviour is measured by packing density obtained during 10 cycles of vibration while the powder is in static mode. Figure 11b shows higher packing densities in the reused powders than in the virgin powders. In general, the average values of apparent and tap density of virgin and reused powders show higher densification in reuse, as listed in Table 6. The loose/packed volume fraction indicates the extent to which the powder particles spread onto the start plate in a homogeneous layer. The high volume fraction exhibited by both the virgin and reused powders indicates favourable conditions for high powder packing on the start plate.

Table 6. Apparent density, tap density and corresponding volume fractions of the virgin and reused powders measured by the RPA.

Material	Apparent Density (g/cm^3)	Loose Volume Fraction (%)	Tap Density (g/cm^3)	Packed Volume Fraction (%)
Virgin	2.39 ± 0.01	48.29 ± 0.17	2.47 ± 0.01	49.97 ± 0.20
Reused	2.55 ± 0.02	51.70 ± 0.31	2.65 ± 0.01	53.56 ± 0.07

4. Conclusions

In this study, the preheating conditions to process the β-Ti21S alloy by Powder Bed Fusion—Electron Beam (PBF-EB) were investigated through sintering using the thermogravimetric (TG) apparatus and experimental PBF-EB builds. Key parameters, such as preheating parameters and temperatures, were identified and validated with the analysis of the morphology of sintered particles. Key conclusions are listed below:

- Preheating conditions: The optimal sintering temperature was identified between 500 °C and 700 °C in sintering using the TG apparatus experiments in combination with simulation by CALPHAD. However, in practice with PBF-EB, a preheating temperature up to 730 °C was the most suitable among the three tested to balance particle adhesion to the start plate without compromising the layering process. Refining at this temperature by adjusting the process parameters will be necessary to balance powder layering and microstructural issues due to overheating above the β-transus temperature.
- Powder reusability: Within the scope of this study, the powder reused after three processing cycles exhibited morphological, particle-size, phase-constitution, and rheological characteristics that remained compatible with further processing under the investigated conditions.

To summarise, this study highlights the importance of the preheating step during the PBF-EB process to control the layering process by adjusting the sintering behaviour without compromising powder reusability.

Author Contributions: Conceptualization, G.R., L.C. and M.G.; methodology, G.R., L.C. and M.G.; formal analysis, G.R. and L.C.; investigation, G.R., L.C. and M.G.; resources, A.S. and E.H.; data curation, G.R. and L.C.; writing—original draft preparation, G.R. and L.C.; writing—review and editing, G.R., L.C., A.S., E.H. and M.G.; visualisation, G.R. and L.C.; supervision, M.G.; funding acquisition, A.S. and E.H. All authors have read and agreed to the published version of the manuscript.

Funding: This research received no external funding.

Institutional Review Board Statement: Not applicable.

Informed Consent Statement: Not applicable.

Data Availability Statement: The raw data supporting the conclusions of this article will be made available by the authors on request.

Acknowledgments: This work was conducted in the framework of the Centre for Additive Manufacturing—Metal (CAM2), supported by the Swedish Governmental Agency of Innovation Systems (Vinnova).

Conflicts of Interest: The authors declare no conflicts of interest.

References

1. Lütjering, G.; Williams, J.C. (Eds.) Beta Alloys. In *Titanium*; Springer: Berlin/Heidelberg, Germany, 2007; pp. 283–336.
2. Dias Corpa Tardelli, J.; Bolfarini, C.; Cândido dos Reis, A. Comparative Analysis of Corrosion Resistance between Beta Titanium and Ti-6Al-4V Alloys: A Systematic Review. *J. Trace Elem. Med. Biol.* **2020**, *62*, 126618. [CrossRef]
3. Pellizzari, M.; Jam, A.; Tschon, M.; Fini, M.; Lora, C.; Benedetti, M. A 3D-Printed Ultra-Low Young's Modulus β-Ti Alloy for Biomedical Applications. *Materials* **2020**, *13*, 2792. [CrossRef]
4. Niinomi, M.; Nakai, M. Titanium-Based Biomaterials for Preventing Stress Shielding between Implant Devices and Bone. *Int. J. Biomater.* **2011**, *2011*, 836587. [CrossRef] [PubMed]
5. Chen, L.-Y.; Cui, Y.-W.; Zhang, L.-C. Recent Development in Beta Titanium Alloys for Biomedical Applications. *Metals* **2020**, *10*, 1139. [CrossRef]
6. Lin, C.; Feng, Z.; Chun, M.; Chen, Y.; Zhang, X.; Hua, J.; Zhang, Z.; Huang, J. Design and Analysis of Porous Root-Analogue-Dental-Implants with a Sine-Wave Structure for Reducing Stress Shielding. *Addit. Manuf. Front.* **2026**, 200324. [CrossRef]
7. Zhang, L.; Song, B.; Choi, S.-K.; Shi, Y. A Topology Strategy to Reduce Stress Shielding of Additively Manufactured Porous Metallic Biomaterials. *Int. J. Mech. Sci.* **2021**, *197*, 106331. [CrossRef]
8. Khorasani, A.M.; Goldberg, M.; Doeven, E.H.; Littlefair, G. Titanium in Biomedical Applications—Properties and Fabrication: A Review. *J. Biomater. Tissue Eng.* **2015**, *5*, 593–619. [CrossRef]
9. Ma, H.Y.; Wang, J.C.; Qin, P.; Liu, Y.J.; Chen, L.Y.; Wang, L.Q.; Zhang, L.C. Advances in Additively Manufactured Titanium Alloys by Powder Bed Fusion and Directed Energy Deposition: Microstructure, Defects, and Mechanical Behavior. *J. Mater. Sci. Technol.* **2024**, *183*, 32–62. [CrossRef]
10. Apaza-Bedoya, K.; Tarce, M.; Benfatti, C.A.M.; Henriques, B.; Mathew, M.T.; Teughels, W.; Souza, J.C.M. Synergistic Interactions between Corrosion and Wear at Titanium-Based Dental Implant Connections: A Scoping Review. *J. Periodontal Res.* **2017**, *52*, 946–954. [CrossRef] [PubMed]
11. Cordeiro, J.M.; Barão, V.A.R. Is There Scientific Evidence Favoring the Substitution of Commercially Pure Titanium with Titanium Alloys for the Manufacture of Dental Implants? *Mater. Sci. Eng. C* **2017**, *71*, 1201–1215. [CrossRef] [PubMed]
12. Zhang, L.-C.; Chen, L.-Y. A Review on Biomedical Titanium Alloys: Recent Progress and Prospect. *Adv. Eng. Mater.* **2019**, *21*, 1801215. [CrossRef]
13. Noronha Oliveira, M.; Schunemann, W.V.H.; Mathew, M.T.; Henriques, B.; Magini, R.S.; Teughels, W.; Souza, J.C.M. Can Degradation Products Released from Dental Implants Affect Peri-Implant Tissues? *J. Periodontal Res.* **2018**, *53*, 1–11. [CrossRef] [PubMed]
14. Mosallanejad, M.H.; Abdi, A.; Karpasand, F.; Nassiri, N.; Iuliano, L.; Saboori, A. Additive Manufacturing of Titanium Alloys: Processability, Properties, and Applications. *Adv. Eng. Mater.* **2023**, *25*, 2301122. [CrossRef]
15. Ng, C.H.; Bermingham, M.J.; Kent, D.; Dargusch, M.S. High Stability and High Strength β-Titanium Alloys for Additive Manufacturing. *Mater. Sci. Eng. A* **2021**, *816*, 141326. [CrossRef]
16. Herzog, D.; Seyda, V.; Wycisk, E.; Emmelmann, C. Additive Manufacturing of Metals. *Acta Mater.* **2016**, *117*, 371–392. [CrossRef]
17. Murr, L.E.; Martinez, E.; Amato, K.N.; Gaytan, S.M.; Hernandez, J.; Ramirez, D.A.; Shindo, P.W.; Medina, F.; Wicker, R.B. Fabrication of Metal and Alloy Components by Additive Manufacturing: Examples of 3D Materials Science. *J. Mater. Res. Technol.* **2012**, *1*, 42–54. [CrossRef]
18. Körner, C. Additive Manufacturing of Metallic Components by Selective Electron Beam Melting—A Review. *Int. Mater. Rev.* **2016**, *61*, 361–377. [CrossRef]
19. Damri, E.; Tiferet, E.; Braun, D.; Ganor, Y.I.; Chonin, M.; Orion, I. Effects of Gas Pressure during Electron Beam Energy Deposition in the EBM Additive Manufacturing Process. *Metals* **2021**, *11*, 601. [CrossRef]
20. Cheng, B.; Price, S.; Lydon, J.; Cooper, K.; Chou, K. On Process Temperature in Powder-Bed Electron Beam Additive Manufacturing: Model Development and Validation. *J. Manuf. Sci. Eng.* **2014**, *136*, 061018. [CrossRef]
21. Weiwei, H.; Wenpeng, J.; Haiyan, L.; Huiping, T.; Xinting, K.; Yu, H. Research on Preheating of Titanium Alloy Powder in Electron Beam Melting Technology. *Rare Met. Mater. Eng.* **2011**, *40*, 2072–2075. [CrossRef]
22. Leung, C.L.A.; Tosi, R.; Muzangaza, E.; Nonni, S.; Withers, P.J.; Lee, P.D. Effect of Preheating on the Thermal, Microstructural and Mechanical Properties of Selective Electron Beam Melted Ti-6Al-4V Components. *Mater. Des.* **2019**, *174*, 107792. [CrossRef]

23. Ye, J.; Renner, J.; Körner, C.; Fu, Z. Electron-Optical Observation of Smoke Evolution during Electron Beam Powder Bed Fusion. *Addit. Manuf.* **2023**, *70*, 103578. [CrossRef]
24. Rizza, G.; Galati, M.; Antonioni, P.; Iuliano, L. Effect of the Sintering Conditions on the Neck Growth during the Powder Bed Fusion with Electron Beam (PBF-EB) Process. *J. Manuf. Mater. Process.* **2023**, *7*, 55. [CrossRef]
25. Zallmann, S.; Fu, Z.; Körner, C. Powder Sintering Kinetics during Electron Beam Based Additive Manufacturing. *Powder Technol.* **2024**, *434*, 119332. [CrossRef]
26. Galati, M.; Rizza, G.; Defanti, S.; Denti, L. Surface Roughness Prediction Model for Electron Beam Melting (EBM) Processing Ti6Al4V. *Precis. Eng.* **2021**, *69*, 19–28. [CrossRef]
27. Landau, E.; Ganor, Y.I.; Braun, D.; Strantza, M.; Matthews, M.J.; Tiferet, E.; Ziskind, G. A Detailed Study of Pre-Heating Effects in Electron Beam Melting Powder Bed Fusion Process. *Addit. Manuf.* **2025**, *99*, 104656. [CrossRef]
28. Landau, E.; Tiferet, E.; Ganor, Y.I.; Ganeriwala, R.K.; Matthews, M.J.; Braun, D.; Chonin, M.; Ziskind, G. Thermal Characterization of the Build Chamber in Electron Beam Melting. *Addit. Manuf.* **2020**, *36*, 101535. [CrossRef]
29. Lee, H.-J.; Ahn, D.-G. Investigation of Elimination of Powder Spreading in Manufacture of Thin and Wide Preheating Beads from Co–Cr Alloy Powders Using a P-Ebeam. *J. Mater. Res. Technol.* **2021**, *14*, 1873–1883. [CrossRef]
30. Galati, M.; Iuliano, L.; Salmi, A.; Atzeni, E. Modelling Energy Source and Powder Properties for the Development of a Thermal FE Model of the EBM Additive Manufacturing Process. *Addit. Manuf.* **2017**, *14*, 49–59. [CrossRef]
31. Xu, J.; Tarafder, P.; Wiberg, A.; Zhang, H.; Moverare, J. Electron Beam Powder Bed Fusion Process Monitoring by In-Melt Electron Analysis. *Addit. Manuf.* **2025**, *109*, 104858. [CrossRef]
32. Rizza, G.; Galati, M.; Iuliano, L. A Phase-Field Study of Neck Growth in Electron Beam Powder Bed Fusion (EB-PBF) Process of Ti6Al4V Powders under Different Processing Conditions. *Int. J. Adv. Manuf. Technol.* **2022**, *123*, 855–873. [CrossRef]
33. Rizza, G.; Galati, M. Powder Bed Fusion with Electron Beam: The Interplay of Sintering, Porosity, and Coordination Number in Modelling the Powder Thermal Conductivity through a Novel Tortuosity Formulation. *Int. J. Heat Mass Transfer* **2024**, *234*, 126055. [CrossRef]
34. Böhm, J.; Breuning, C.; Markl, M.; Körner, C. A New Approach of Preheating and Powder Sintering in Electron Beam Powder Bed Fusion. *Int. J. Adv. Manuf. Technol.* **2024**, *133*, 3769–3784. [CrossRef]
35. Ortmann, R.; Hankel, J.; Grimm, T.; Röttger, A.; Sehrt, J.T. Powder Bed Fusion of Pure Copper Using an Electron Beam—Achieving High Conductivity by Real-Time Process Monitoring and Control. *MATEC Web Conf.* **2024**, *406*, 5001. [CrossRef]
36. Takase, A.; Ishimoto, T.; Suganuma, R.; Nakano, T. Surface Residual Stress and Phase Stability in Unstable β-Type Ti–15Mo–5Zr–3Al Alloy Manufactured by Laser and Electron Beam Powder Bed Fusion Technologies. *Addit. Manuf.* **2021**, *47*, 102257. [CrossRef]
37. Sun, S.-H.; Hagihara, K.; Ishimoto, T.; Suganuma, R.; Xue, Y.-F.; Nakano, T. Comparison of Microstructure, Crystallographic Texture, and Mechanical Properties in Ti–15Mo–5Zr–3Al Alloys Fabricated via Electron and Laser Beam Powder Bed Fusion Technologies. *Addit. Manuf.* **2021**, *47*, 102329. [CrossRef]
38. Chen, B.; Lin, B.; Zhang, Z.; Jia, J.; Liu, W.; Wen, Z.; Sui, T.; Yan, S. Sintering Kinetics and Performance Evolution of Silicon-Rich Mullite Ceramics via Deformation-Thermogravimetric Synchronous Analysis. *J. Alloys Compd.* **2025**, *1042*, 184161. [CrossRef]
39. Wendel, J.; Manchili, S.K.; Cao, Y.; Hryha, E.; Nyborg, L. Evolution of Surface Chemistry during Sintering of Water-Atomized Iron and Low-Alloyed Steel Powder. *Surf. Interface Anal.* **2020**, *52*, 1061–1065. [CrossRef]
40. Hidayanti, F.; Pusparasmi, D.A.; Lazuardi, N. Feedstock Characterization with Thermal Gravimetric Analysis (TGA) and Scanning Electron Microscopy—Energy Dispersive x-Ray Spectroscopy (SEM-EDX) of Titanium Alloy for Metal Injection Molding Technique. *AIP Conf. Proc.* **2020**, *2262*, 50005. [CrossRef]
41. de Oro Calderon, R.; Gierl-Mayer, C.; Danninger, H. Thermoanalytical Techniques for Characterizing Sintering Processes in Ferrous Powder Metallurgy. *J. Therm. Anal. Calorim.* **2023**, *148*, 1309–1320. [CrossRef]
42. Galati, M.; Defanti, S.; Saboori, A.; Rizza, G.; Tognoli, E.; Vincenzi, N.; Gatto, A.; Iuliano, L. An Investigation on the Processing Conditions of Ti-6Al-2Sn-4Zr-2Mo by Electron Beam Powder Bed Fusion: Microstructure, Defect Distribution, Mechanical Properties and Dimensional Accuracy. *Addit. Manuf.* **2022**, *50*, 102564. [CrossRef]
43. Sjöström, W.; Botero, C.; Jimenez-Piqueo, E. Melting Ceramic Al2O3 Powder by Electron Beam Powder Bed Fusion. *Prog. Addit. Manuf.* **2024**, *9*, 1523–1535. [CrossRef]
44. Drescher, P.; Reimann, T.; Seitz, H. Investigation of Powder Removal of Net-Structured Titanium Parts Made from Electron Beam Melting. *Int. J. Rapid Manuf.* **2014**, *4*, 81. [CrossRef]
45. Montelione, A.; Ghods, S.; Schur, R.; Wisdom, C.; Arola, D.; Ramulu, M. Powder Reuse in Electron Beam Melting Additive Manufacturing of Ti6Al4V: Particle Microstructure, Oxygen Content and Mechanical Properties. *Addit. Manuf.* **2020**, *35*, 101216. [CrossRef]
46. Cao, Y.; Delin, M.; Kullenberg, F.; Nyborg, L. Surface Modification of Ti-6Al-4V Powder during Recycling in EBM Process. *Surf. Interface Anal.* **2020**, *52*, 1066–1070. [CrossRef]

47. Cordova, L.; Raza, A.; Hryha, E. Rheological Behavior of Inconel 718 Powder for Electron-Beam Melting. *Metals* **2022**, *12*, 1231. [CrossRef]
48. Schur, R.; Ghods, S.; Wisdom, C.; Pahuja, R.; Montelione, A.; Arola, D.; Ramulu, M. Mechanical Anisotropy and Its Evolution with Powder Reuse in Electron Beam Melting AM of Ti6Al4V. *Mater. Des.* **2021**, *200*, 109450. [CrossRef]
49. Ghods, S.; Schultz, E.; Wisdom, C.; Schur, R.; Pahuja, R.; Montelione, A.; Arola, D.; Ramulu, M. Electron Beam Additive Manufacturing of Ti6Al4V: Evolution of Powder Morphology and Part Microstructure with Powder Reuse. *Materialia* **2020**, *9*, 100631. [CrossRef]
50. Tang, H.P.; Qian, M.; Liu, N.; Zhang, X.Z.; Yang, G.Y.; Wang, J. Effect of Powder Reuse Times on Additive Manufacturing of Ti-6Al-4V by Selective Electron Beam Melting. *JOM* **2015**, *67*, 555–563. [CrossRef]
51. Borrelli, R.; Bellini, C.; Berto, F.; Di Cocco, V.; Foti, P.; Iacoviello, F.; Mocanu, L.P.; Pirozzi, C.; Razavi, N.; Franchitti, S. The Impact of Ti6Al4V Powder Reuse on the Quality of Electron Beam Powder Bed Fusion Parts. *Prog. Addit. Manuf.* **2024**, *9*, 1475–1490. [CrossRef]
52. Cordova, L.; Campos, M.; Tinga, T. Revealing the Effects of Powder Reuse for Selective Laser Melting by Powder Characterization. *JOM* **2019**, *71*, 1062–1072. [CrossRef]
53. Ferreira, B.T.; Monteiro, J.; Borille, A.; Leite, M.; Ribeiro, I. Reuse Powder Impacts in Additive Manufacturing for Aeronautical Parts. *Int. J. Adv. Manuf. Technol.* **2025**, *141*, 2027–2062. [CrossRef]
54. Cordova, L.; Bor, T.; de Smit, M.; Campos, M.; Tinga, T. Measuring the Spreadability of Pre-Treated and Moisturized Powders for Laser Powder Bed Fusion. *Addit. Manuf.* **2020**, *32*, 101082. [CrossRef]
55. *B822-02*; Standard Test Method for Particle Size Distribution of Metal Powders and Related Compounds by Light Scattering. ASTM: West Conshohocken, PA, USA, 2022.
56. Ivasishin, O.M.; Markovsky, P.E.; Matviychuk, Y.V.; Semiatin, S.L.; Ward, C.H.; Fox, S. A Comparative Study of the Mechanical Properties of High-Strength β-Titanium Alloys. *J. Alloys Compd.* **2008**, *457*, 296–309. [CrossRef]
57. Mantri, S.A.; Choudhuri, D.; Behera, A.; Hendrickson, M.; Alam, T.; Banerjee, R. Role of Isothermal Omega Phase Precipitation on the Mechanical Behavior of a Ti-Mo-Al-Nb Alloy. *Mater. Sci. Eng. A* **2019**, *767*, 138397. [CrossRef]
58. Ghosh, M.; Bhanumurthy, K.; Kale, G.B.; Krishnan, J.; Chatterjee, S. Diffusion Bonding of Titanium to 304 Stainless Steel. *J. Nucl. Mater.* **2003**, *322*, 235–241. [CrossRef]
59. Macias-Sifuentes, M.A.; Xu, C.; Sanchez-Mata, O.; Kwon, S.Y.; Atabay, S.E.; Muñiz-Lerma, J.A.; Brochu, M. Microstructure and Mechanical Properties of β-21S Ti Alloy Fabricated through Laser Powder Bed Fusion. *Prog. Addit. Manuf.* **2021**, *6*, 417–430. [CrossRef]
60. Lin, Z.; Dadbakhsh, S.; Rashid, A. Developing Processing Windows for Powder Pre-Heating in Electron Beam Melting. *J. Manuf. Process.* **2022**, *83*, 180–191. [CrossRef]
61. Hryha, E.; Shvab, R.; Bram, M.; Bitzer, M.; Nyborg, L. Surface Chemical State of Ti Powders and Its Alloys: Effect of Storage Conditions and Alloy Composition. *Appl. Surf. Sci.* **2016**, *388*, 294–303. [CrossRef]

Disclaimer/Publisher's Note: The statements, opinions and data contained in all publications are solely those of the individual author(s) and contributor(s) and not of MDPI and/or the editor(s). MDPI and/or the editor(s) disclaim responsibility for any injury to people or property resulting from any ideas, methods, instructions or products referred to in the content.